Rock Mechanics and Rock Engineering (2020) 53:5795–5808
https://doi.org/10.1007/s00603-020-02224-x

TECHNICAL NOTE

Analysis of Fractured Rock Permeability Evolution Under Unloading Conditions by the Model of Elastoplastic Contact Between Rough Surfaces

Y. Zhao[1,2] · C. L. Wang[1,2] · J. Bi[1,2]

Received: 20 July 2019 / Accepted: 6 August 2020 / Published online: 14 August 2020

Keywords Rock fracture · Permeability · Unload · Elastoplastic contact

List of Symbols

a	Contact area
a_{ec}	Elastic critical contact area
a_{epc}	Elastoplastic critical contact area
a_l	The largest contact area of asperity
A	Sample cross-sectional area
A_r	The total real contact area
K	Permeability
C	Water compressibility
C_f	Fracture compressibility
E	Young's moduli
F	Contact load
F_{ec}	Elastic critical contact load
F_{max}	Maximum contact load before unloading
F_{ne}	Contact load for elastic deformation
F_{nep}	Contact load for elastoplastic deformation
H	Hardness of the asperity
K	Hardness coefficient
L	Sample length
R	Radius of asperity
S_d	Maximum depth of valleys
S_h	Maximum absolute height
S_m	Arithmetical mean height
S_p	Maximum peak height
V_u	Volume of the upstream chamber
V_d	Volume of the downstream chamber
Y	The yield strength of material
α	The fitting parameter of the pressure decay curve
δ	Normal displacement
μ	Fluid viscosity
ν	Poisson's ratio
ω	Deformation of the asperity
ω_c	Critical deformation at the inception of plastic deformation
ω_{max}	Maximum contact interference before unloading
ω_{res}	Residual contact interference after complete unloading

1 Introduction

Underground excavations usually cause stress unloading of the surrounding rock masses. Due to the stress release, these engineering activities may lead the rock mass to deform and produce macroscopic fractures (Qiu et al. 2014; Zhang et al. 2016, 2020; Zhao et al. 2019a), which increases the rock mass permeability significantly and, finally, triggers engineering problems such as mine water inrush and water loss (Li et al. 2019a, b). Therefore, a knowledge of changes in the permeability of rock joints that result from the stresses unloading around geotechnical engineering projects is crucially important.

The relationships between stress and permeability of fractured rock masses have been extensively studied in the last two decades (Zhao et al. 2003, 2017; Chen et al. 2015; Vogler et al. 2016). It is found that permeability evolution is closely related to the effective stress. As the effective stress increases, rock permeability decreases exponentially (Zhao et al. 2019b). At present, abundant models were proposed to predict the rock permeability evolution with stress variation. Shi and Durucan (2004) presented a model for describing changes in fracture permeability during the drawdown in terms of the prevailing effective horizontal stresses. Liu and Rutqvist (2010)

✉ C. L. Wang
chaolinwang@126.com

[1] College Civil Engineering, Guizhou University, Guiyang 550025, Guizhou, China

[2] Guizhou Provincial Key Laboratory of Rock and Soil Mechanics and Engineering Safety, Guiyang 550025, Guizhou, China

developed a new permeability model with consideration of internal swelling stress. Wang et al. (2014) presented an analytical model of describing anisotropic permeability evolution of coal with effective stress variation. Connell (2016) provided a simple extension of the exponential model of rock permeability to include the independent effects of pore and confining pressures and the sorption strain. However, most of these permeability models are derived from the elastic deformation assumption. This may be suitable for intact rock under low-stress conditions. However, for fractured rock mass or broken rock sample, re-crushing, re-arrangement, and compressional deformation of asperity or particles occur in the loading process, which leads to a drastic permeability reduction (Zhang et al. 2017). Usually, crushing and re-arrangement of asperity in rough surfaces are irreversible. During the unloading process, only the permeability loss caused by the elastic asperity deformation can be recovered. The plastic deformation, such as crushing and re-arrangement of asperity, will cause irreversible permeability loss. Abundant experimental studies have proved that in the unloading process, permeability is always less than that obtained during loading under the same effective stress. Yang et al. (2018) investigated the anisotropic permeability of coal subjected to cyclic loading and unloading and found that irreversible permeability occurred during the unloading process. Zhang et al. (2018) conducted a set of experiments on fractured coal samples under cyclic loading and unloading. The test results showed that permeability loss caused by the deformation of fracture surfaces was very difficult to compensate for in the process of unloading. Jiang et al. (2017) found that the AE (acoustic emission) signal appeared in the whole unloading process due to the difference between the plastic irrecoverable region and the surrounding elastic recovery region of the coal sample. According to these experimental studies, the unloading behaviors of rock deformation and permeability are substantially different from the behaviors under loading conditions. But, to the best knowledge of the authors, theoretical models for addressing permeability evolution under unloading conditions are very limited. Therefore, in this paper, the deformation and permeability change of rock sample containing a single rough-walled fracture under unloading conditions are experimentally investigated. Elastoplastic contact of asperity in rough surfaces under unloading conditions is analyzed, which is further implanted into the permeability model to predict fractured rock permeability evolution under unloading conditions.

2 Laboratory Experimental Analysis

2.1 Sample Preparation and Measurement of Morphological Parameters

Black limestone blocks used in the experimental works were obtained from the Feisanduan limestone formation in southwest Hubei Province (China). Three 50-mm-diameter cylindrical cores (namely samples L01, L02, and L03) were retrieved from a limestone block. Both ends of the cylindrical core were trimmed to obtain a sample of length 100 mm. Then, a single vertical fracture was generated at the center of the samples along the axial sample direction following the method of Zhao et al. (2017). Note that the samples were covered by a heat-shrinkable sleeve to keep the two halves of fractured sample together during fracture generation. Figure 1a–c shows the prepared samples with a single rough-walled fracture.

A high-resolution noncontact 3D morphology scanner system is utilized to measure the fracture surfaces' topography before and after testing. Data collection was automatically completed by the morphology instrument with a precision of 0.002 mm in the X, Y, and Z directions. The scanned data of the fracture surfaces were digitized, as shown in Fig. 1.

Four main statistical parameters: maximum peak height (S_p), maximum depth of valleys (S_d), maximum absolute height (S_h), and arithmetical mean height (S_m), were adopted to quantify the morphology of fracture surface (Chen et al. 2010; Singh et al. 2015; Zhao et al. 2017). These statistical parameters can effectively describe the fracture surface roughness. The larger the values of these parameters are, the rougher the fracture surface is. The expressions of these parameters are as follows. The maximum peak height S_p is the height between the reference plane and the highest peak:

$$S_p = \max\left(S_{p1}, S_{p2}, \ldots, S_{pn}\right) \tag{1}$$

where S_{pi} ($i = 1,2,\ldots, n$) is the height between the reference plane and the ith peak, and n is the total peak number. The maximum depth of valleys S_d is the depth between the deepest valley and the reference plane:

$$S_d = \max\left(S_{d1}, S_{d2}, \ldots, S_{dn}\right) \tag{2}$$

where S_{di} ($i = 1,2,\ldots, n$) is the depth between the reference plane and the ith valley. The maximum absolute height S_h is the height between the highest peak and the deepest valley:

$$S_h = S_p + S_d \tag{3}$$

The mean surface roughness can be characterized by the arithmetic mean height S_m:

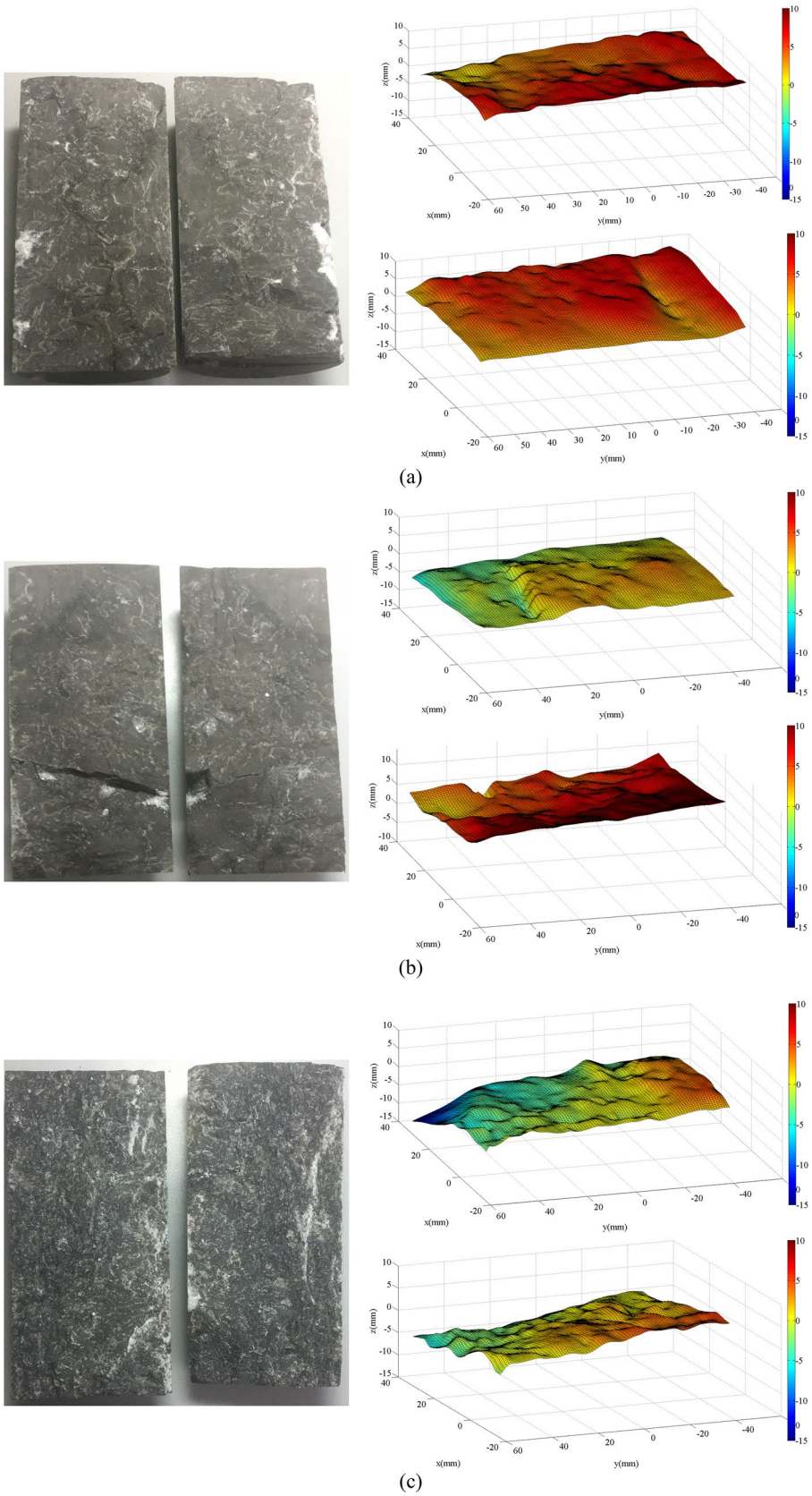

Fig. 1 Prepared samples and 3D surface profiles of the fracture surfaces, **a–c** corresponding to samples L01, L02, and L03, respectively

$$S_m = \frac{1}{A}\iint_A |z(x,y)|dxdy \tag{4}$$

where $z(x, y)$ is the asperity height at the location (x, y) and A is the area of the fracture surface projected onto the horizontal plane.

2.2 Experimental Procedure

A fluid flow and triaxial rock mechanics test system, shown in Fig. 2, is used for the permeability test. The test system includes five main units: triaxial cell, loading unit, deformation and pressure monitoring unit, water supply unit, and computerized data-acquisition unit. The experimental setup has the maximum axial loading capacity of 1000 kN, the maximum confining pressure of 60 MPa, and the maximum pore water pressure of 40 MPa. The pressure pulse decay method is used to measure rock permeability. In the permeability tests, the maximum axial and confining stresses were set as 20 MPa to simulate the conditions occurring 500 m below in the earth's crust. During the test, the sample was circumferentially sealed in plastic pipe, placed on the base pedestal of the triaxial cell, and connected to the upstream and downstream water reservoirs. The confining pressure was first loaded to the predetermined value, and then axial stress was loaded to 20 MPa at a rate of 1 MPa/min. Then, the fractured samples were loaded from confining pressure of 6–20 MPa in gradual levels of 2 MPa, at a loading rate of 0.5 MPa/min. After reaching the maximum stress of 20 MPa, confining pressure was unloaded to 6 MPa in gradual levels of 2 MPa, at a rate of 0.5 MPa/min. Permeability was measured during each confining pressure loading and unloading steps. In the permeability tests, water pressure should be smaller than the confining pressure to avoid fluid flow from the gap between the rock sample and the plastic pipe. Therefore, in this paper, the initial water pressure was set as 2 MPa (Davy et al. 2007; Dong et al. 2010). After applying the initial water pressure to the system, a pulse pressure of 0.2 MPa was applied in the upstream chamber, which made the water flow from top to bottom through the fracture. The

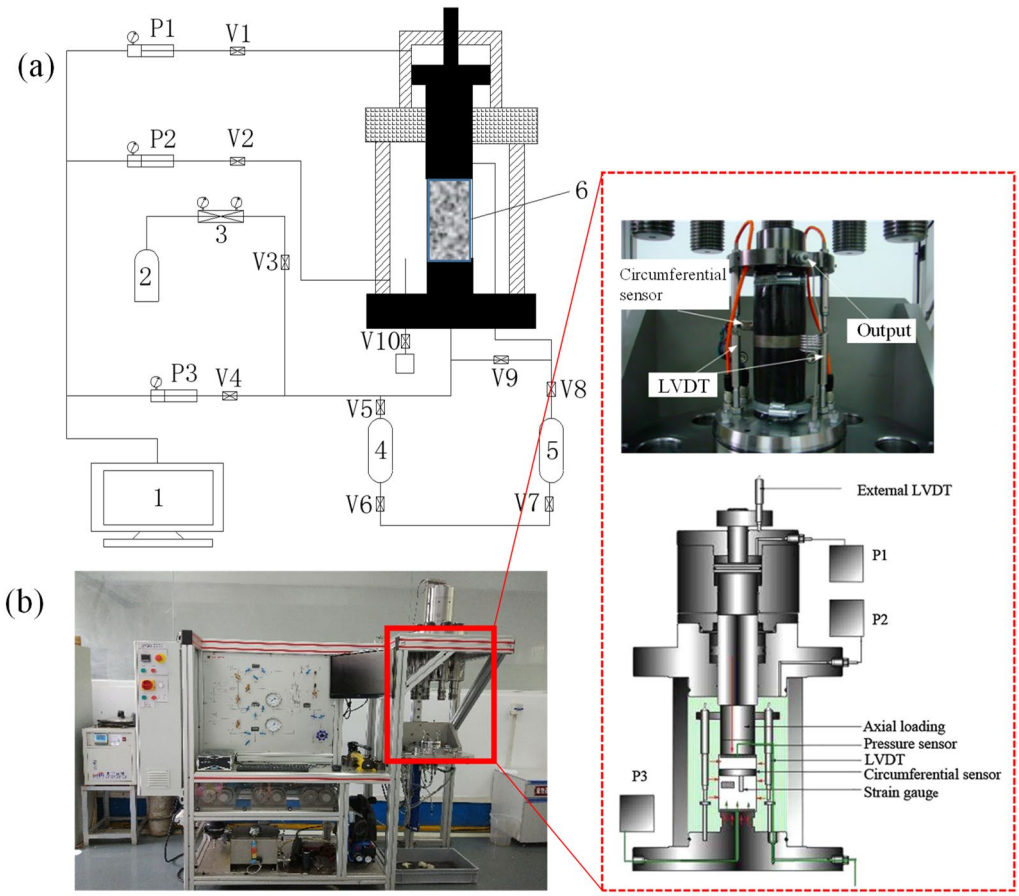

Fig. 2 **a** Sketch of the triaxial seepage system for rock (P1—axial loading unit; P2—confining pressure unit; P3—water pressure unit; 1—computerized data-acquisition unit; 2—water reservoir; 3—relief valve; 4—upstream chamber; 5—downstream chamber; 6—sample; and V1–V10—switch); **b** picture of the testing system

differential pressure data versus flow time data were automatically recorded until equilibrium is attained by the testing system for determining permeability. Calculation formula for permeability in the pressure pulse decay test can be written as (Brace et al. 1968; Wang et al. 2019):

$$\alpha = \frac{kA}{c\mu L}\left(\frac{1}{V_u} + \frac{1}{V_d}\right) \tag{5}$$

where k is the permeability; $\propto$ is the fitting parameter based on fitting of the pressure decay verse flow time data with an exponential equation; A is sample cross-sectional area, L is sample length; c is the compressibility of water; μ is fluid viscosity; and V_u and V_d are the volumes of upstream and downstream chamber, respectively.

2.3 Experimental Results

Figure 3 shows the obtained permeabilities of fractured rock samples. For the three tested samples, the fracture permeability decreases sharply with the effective stress under loading conditions due to the decrease in fracture aperture. As confining pressure increased from 6 to 20 MPa, sample permeability decreased from 13.72×10^{-16} to 2.09×10^{-16} m^2, 30.72×10^{-16} to 2.56×10^{-16} m^2, and 27.1×10^{-16} to 1.3×10^{-16} m^2 for samples L01, L02, and L03, respectively. In the unloading process, the measured permeability recovers, but all the values are less than that obtained during loading under the same stress conditions. The permeability reduction during the loading process consists of two components: fracture surfaces deformation and pore space squeeze due to fracture surfaces contact crush and friction slipping. At the beginning of the loading process, the two fracture surfaces are linearly compacted with elastic deformations. When the loading stress increases to the asperity contact strength of the two fracture surfaces, the asperity contacts are crushed and reconsolidated, and slide occurs between the two surfaces (as shown in Fig. 4b). Meanwhile, the pulverized particles begin to fill the fracture space and some particles are washed away with water. As more fracture contact is broken, the pulverized particles gradually fill the fracture. As a result, the void between the two fracture surfaces substantially reduces. During the unloading process, the elastic fracture deformations can be recovered while mutual embedding of fracture surfaces and pulverized particles filling are very difficult to compensate, as shown schematically in Fig. 4c. This leads to a great loss of fracture permeability. Note that the penetration channel may expand due to pulse water pressure. But the magnitude of fracture expansion is much smaller than the magnitude of void reduction due to the application of confining pressure (Zhao et al. 2017).

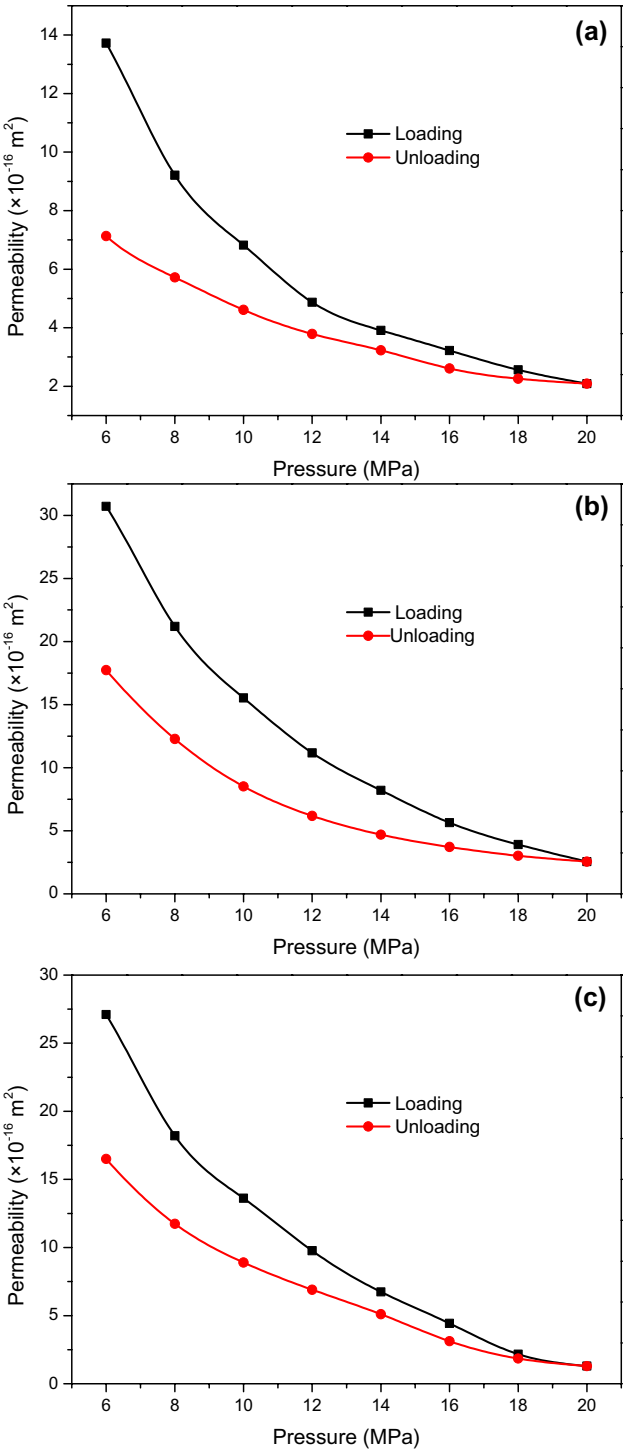

Fig. 3 Permeability results of the testing samples during the loading and unloading processes: **a** sample L01, **b** sample L02, and **c** sample L03

Fracture deformation is measured synchronously by a circumferential extensometer placed in the mid-height of the sample. Figure 5 shows the evolution of fracture deformation under loading and unloading conditions. As shown

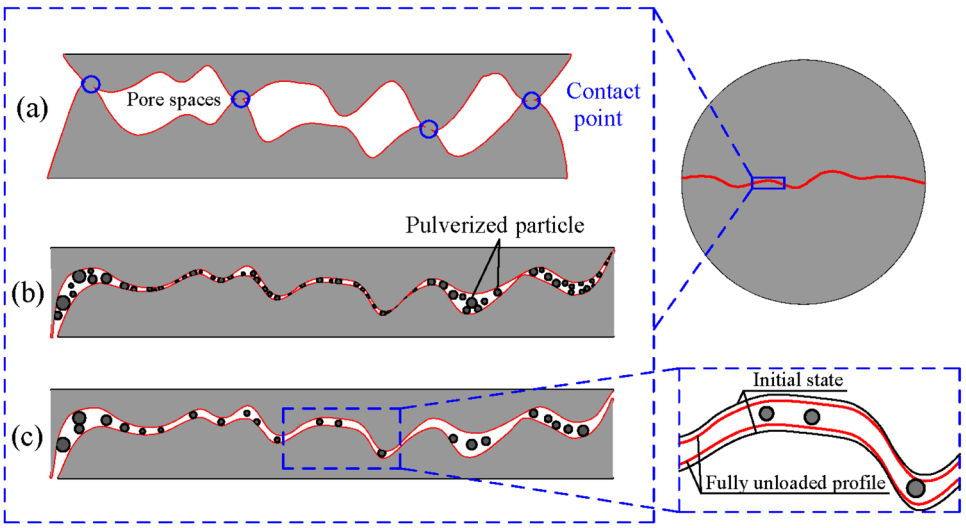

Fig. 4 Schematic of fracture compaction at: **a** initial state, **b** under loading conditions; and **c** under unloading conditions (Zhang et al. 2018)

in Fig. 5, fracture deformation is decreased at a decreasing rate as the effective stress increases. It is noted that fracture deformation under unloading conditions is smaller than the corresponding deformation under loading conditions. This further implies the existence of plastic deformation of the fracture.

Fracture aperture has a significant influence on flow behavior. Changes in mechanical aperture were estimated following the method of Vogler et al. (2016) in which they used the volume change of the confining fluid to quantify relative mechanical aperture. Hydraulic aperture was calculated using the cubic law and the parallel plate model (Zhao et al. 2017). Figure 6 shows the changes in mechanical aperture and hydraulic aperture with confining pressure for the three fractured samples. Mechanical aperture changes are more than one order magnitude larger than hydraulic aperture change for the tested three samples. There is an irreversible reduction in both mechanical aperture and hydraulic aperture after the loading and unloading processes. For example, after the loading and unloading processes, the hydraulic aperture of samples L01, L02, and L03 decreased by 38.7%, 31.6%, and 28.2%, respectively.

Contact areas can significantly affect the fracture interior geometries such as blocking the connected void spaces, decreasing the effective apertures, and adding more flow resistance (Zhang and Chai 2020). Based on the scanned topography, we first calculate the normal displacement of fracture during loading and unloading through the elastoplastic contact deformation principle (shown in Sect. 3.1). Then, the distribution of initial fracture aperture is determined using the upper and lower surface heights data (Sharifzadeh et al. 2008). Therefore, we can obtain the aperture distribution under loading and unloading. Location areas where apertures are equal to or less than zero represent contact areas. The contact characteristics are represented by the contact area ratio, which is defined as the ratio of total area of contact regions over the apparent area of the whole fracture specimen (Li et al. 2008, 2019a, b). The evolution of contact ratio during loading and unloading is shown in Fig. 7 for sample L01. At the same confining pressure condition, the contact ratio under unloading is always greater than the contact ratio under loading. Their difference is small in the early stage of unloading process, which gradually increases with the unloading of confining pressure. This mainly because the deformation cannot be recovered fully during unloading, which leads to more contact areas than loading at the same stress condition. This mechanism can be well explained by the elastoplastic contact theory applied to rough-walled surfaces (shown in Sect. 3.1).

Table 1 shows the morphological parameters for fracture surfaces before and after testing. For the three tested samples, the maximum peak height S_p and the maximum depth of valleys S_d both experienced a substantial reduction after permeability tests, leading to a significant decrease in the maximum absolute height S_h. This phenomenon is influenced by asperity crushing which decreases the peak height of fracture surface. Meanwhile, the breaking of individual grains and asperities can lead to valleys of fracture that fill with gouge material, resulting in a decrease in the depth of valleys. The arithmetic mean height S_m also experienced a reduction after permeability tests, indicating that discreteness of the asperity heights and the deviation of the rough surface from the reference plane have decreased. The results above clearly illustrate that the surface roughness decreases as a result of compression due to the confining pressure and scouring due to the flowing water.

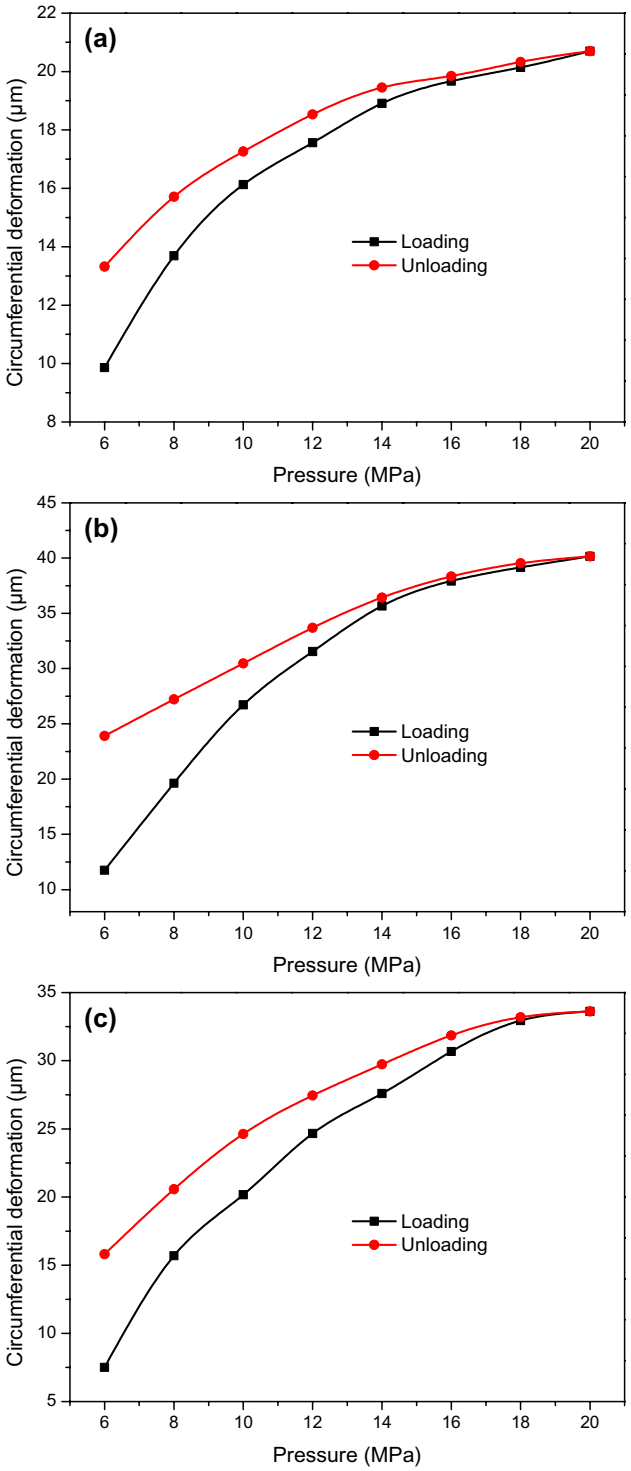

Fig. 5 Deformation of samples under loading and unloading predicted curves and the experimental results: **a** sample L01, **b** sample L02, and **c** sample L03

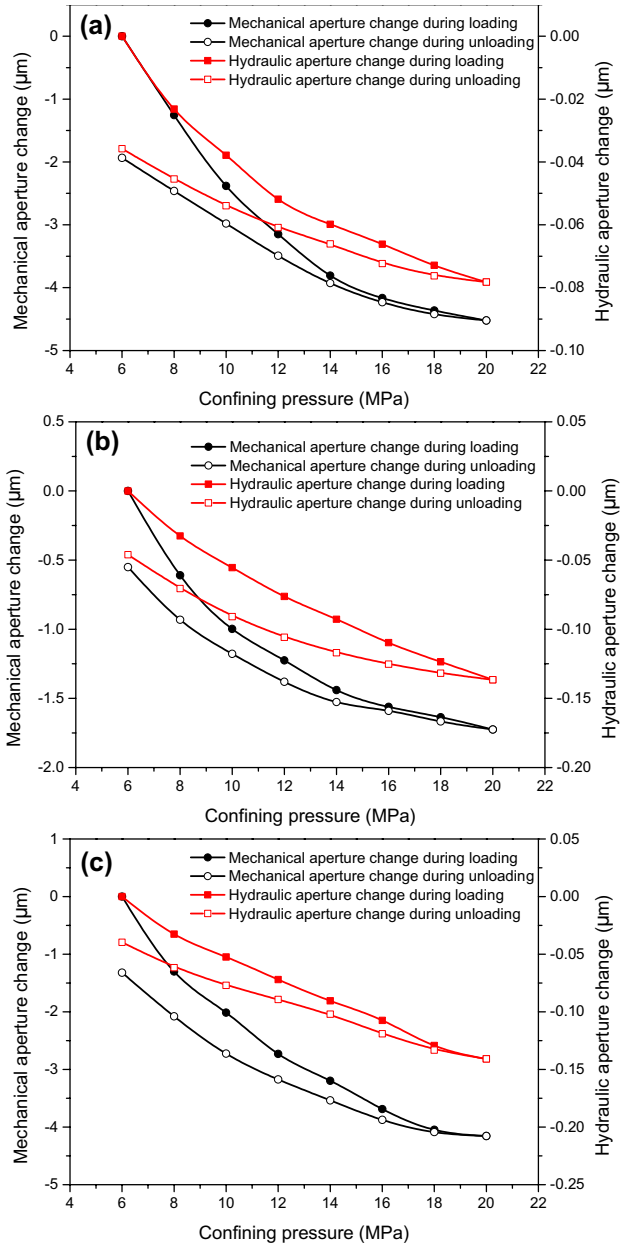

Fig. 6 Changes in mechanical aperture and hydraulic aperture with confining pressure for: **a** sample L01, **b** sample L02, and **c** sample L03

3 Theoretical Analysis of Permeability Evolution in the Laboratory Test

In order to illustrate the permeability evolution of the fractured rock mass during the unloading process, the asperity deformation of the rough surface was calculated by the elastoplastic contact deformation principle.

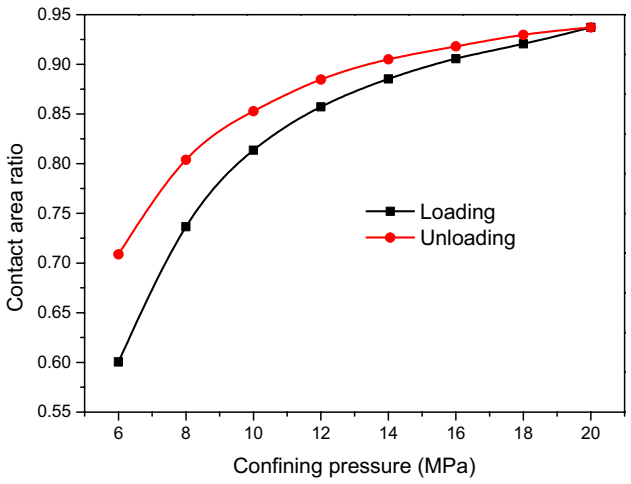

Fig. 7 Evolution of contact area ratio during loading and unloading for sample L01

3.1 Elastoplastic Contact of Rock Joint Under Unloading

Realistic contact of natural rock joint can be transformed into the contact between a smooth surface and a rough surface composed of the two rough surfaces, as shown in Fig. 8 (Brown and Scholz 1985, 1986; Cook 1992; Tang et al. 2017). To obtain the analytical solution of the contact of rock joint, Greenwood and Williamson (1966) assumed that rough surface is covered uniformly with identical, spherically shaped asperities following a Gaussian statistical distribution. The classical Hertz solution deals with the elastic contact problem of a sphere and a rigid flat, which gives contact load as:

$$F_{ne} = \frac{4}{3} E R^{1/2} \delta^{3/2} \tag{6}$$

where E is the Young's moduli, R is the radius of asperity, and δ is the applied normal displacement. However, as described earlier, the original un-deformed rough surfaces are not fully recovered under unloading and residual stresses and displacements remain locked in. This indicates that the elastoplastic contact theory should be used in this problem.

Figure 9 shows the sketch of elastoplastic contact of the unloading problem (Yuan et al. 2018). As can be seen from the figure, the profile of the unloaded asperity is characterized by two parameters: a residual deformation ω_{res} and a residual nonuniform curvature with a radius R_{res} at its summit. Obviously, the residual deformation and

Table 1 Morphological parameters for fracture surfaces of sample L01, L02, and L03 before and after permeability tests

Parameter	L01			L02			L03		
	Before test	After test	Change	Before test	After test	Change	Before test	After test	Change
S_p (mm)	5.73	4.94	0.79	4.05	3.11	0.94	5.41	4.29	1.12
S_d (mm)	4.98	3.18	1.8	6.11	1.63	4.48	12.45	9.88	2.57
S_h (mm)	10.71	8.12	2.59	10.17	4.74	5.43	17.86	14.17	3.69
S_m (mm)	1.69	1.44	0.25	1.73	1.52	0.21	2.73	2.25	0.48

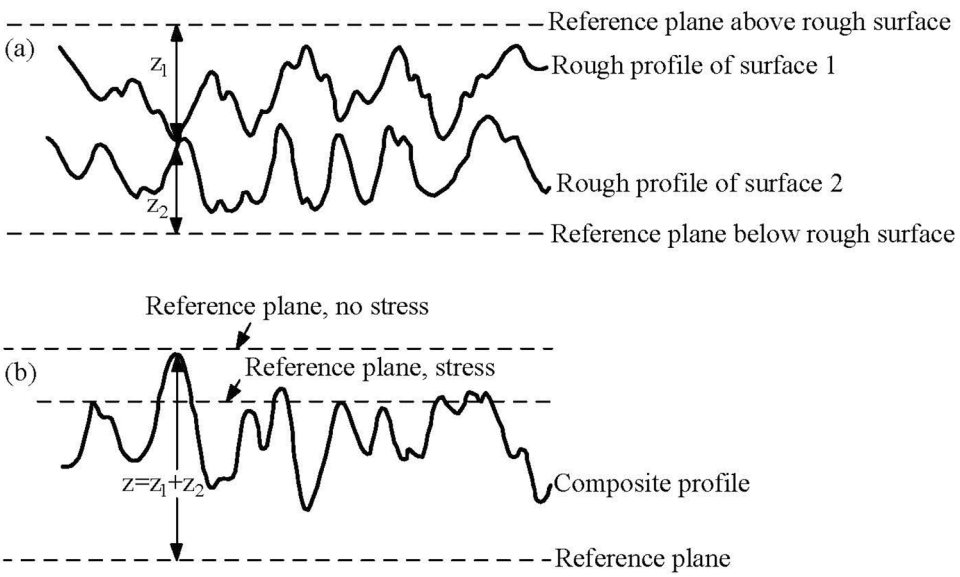

Fig. 8 **a** Sketch of two rough surface profiles of a joint and **b** sketch of a composite topography after Cook (1992)

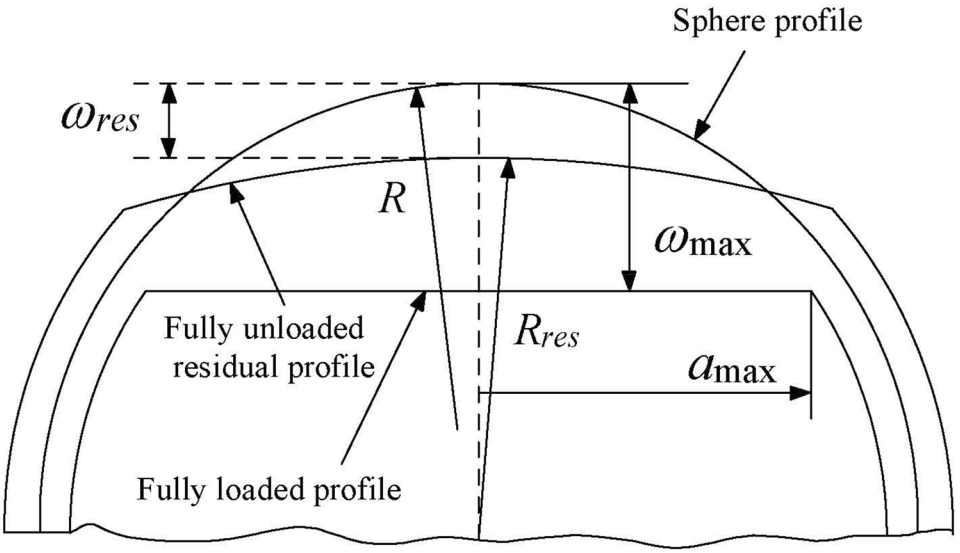

Fig. 9 Sketch of elastoplastic contact of the unloading problem (Yuan et al. 2018)

deformed profile of the unloaded asperity depend on the loading level with associated parameter of the maximum deformation or the maximum contact load from which the unloading process started.

A critical deformation which describes the transition from the elastic to the elastoplastic deformation regime is defined as (Chang et al. 1987; Kogut and Etsion 2002; Yuan et al. 2017):

$$\omega_c = \left(\frac{\pi KH}{2E}\right)^2 R \tag{7}$$

where K is hardness coefficient, $K = 0.454 + 0.41\nu$ (Chang et al. 1988), H is the hardness of the asperity, $H = 2.8Y$, and Y is the yield strength of material. Based on the parameter ω_c, Kogut and Etsion (2002) summarized the asperity deformation as elastic deformation ($\omega \le \omega_c$), elastoplastic deformation (including first elastoplastic deformation regime ($\omega_c < \omega \le 6\omega_c$) and the second elastoplastic deformation regime, $6\omega_c < \omega \le 110\omega_c$), and full plastic deformation ($\omega > 110\omega_c$).

For $\omega \le \omega_c$, the elastic contact load on the asperity under the unloading process is given in Eq. (6). The contact area between the asperity and the rigid surface in the elastic deformation regime is given by the Hertzian theory to be (Johnson 1985)

$$a = \pi R\omega \tag{8}$$

For the elastoplastic contact problem, the contact load and contact area on the asperity during unloading can be written as (Etsion et al. 2005):

$$F_{nep} = F_{\max}\left(\frac{\omega - \omega_{res}}{\omega_{\max} - \omega_{res}}\right)^{1.5(\omega_{\max}/\omega_c)^{-0.0331}} \tag{9}$$

$$a_{nep} = a_{\max}\left(\frac{\omega - \omega_{res}}{\omega_{\max} - \omega_{res}}\right)^{(\omega_{\max}/\omega_c)^{-0.12}} \tag{10}$$

where the subscript *nep* donates the elastoplastic regime and $a_{\max}$ and $F_{\max}$ are the contact area and contact load from which the unloading process started, respectively. Therefore, $a_{\max}$ and $F_{\max}$ can be calculated during the loading process. Kogut and Etsion (2002) presented a solution for elastoplastic deformation contact problem during loading, which gives

$$\frac{a^1_{\max}}{a_{ec}} = 0.93\left(\frac{\omega_{\max}}{\omega_c}\right)^{1.136},\ \frac{F^1_{\max}}{F_{ec}} = 1.03\left(\frac{\omega_{\max}}{\omega_c}\right)^{1.425},\ \text{for } \omega_c < \omega_{\max} \le 6\omega_c \tag{11}$$

$$\frac{a^2_{\max}}{a_{ec}} = 0.94\left(\frac{\omega_{\max}}{\omega_c}\right)^{1.146},\ \frac{F^2_{\max}}{F_{ec}} = 1.40\left(\frac{\omega_{\max}}{\omega_c}\right)^{1.263},\ \text{for } 6\omega_c < \omega_{\max} \le 110\omega_c \tag{12}$$

where a_{ec} and F_{ec} are the contact area and contact load for $\omega = \omega_c$, respectively (i.e., $a_{ec} = \pi R\omega_c$, $F_{ec} = \frac{4}{3}ER^{1/2}\omega_c^{3/2}$). Superscripts 1 and 2 indicate the first elastoplastic deformation regime and the second elastoplastic deformation regime, respectively. Substituting Eqs. (10), (11), and (12) into Eq. (9) yields the contact load on asperity during unloading:

$$F_{nep}^{1} = \frac{2.06KH}{3} a_{ec} \left(\frac{\omega_{\max}}{\omega_c}\right)^{1.425} \left(\frac{a}{0.93a_{ec}\left(\omega_{\max}/\omega_c\right)^{1.136}}\right)^{1.5\left(\omega_{\max}/\omega_c\right)^{0.0869}} \tag{13}$$

$$F_{nep}^{2} = \frac{2.8KH}{3} a_{ec} \left(\frac{\omega_{\max}}{\omega_c}\right)^{1.236} \left(\frac{a}{0.94a_{ec}\left(\omega_{\max}/\omega_c\right)^{1.146}}\right)^{1.5\left(\omega_{\max}/\omega_c\right)^{0.0869}} \tag{14}$$

The full plastic deformation occurs in a single asperity for $\omega > 110\omega_c$. Since asperity does not have a recovery process under full plastic contact condition, there are no contact area and contact load in the unloading process when the loading stress is removed. Therefore, the full plastic contact problem ($\omega > 110\omega_c$) under the unloading process is not included in this paper.

Figure 10 shows the relationship of contact area and contact load for a single asperity during loading and unloading. When the ratio of asperity deformation over asperity height ($\omega_{\max}$/h) is 0.3, only elastic deformation occurs and the two curves of contact area versus contact load under loading and unloading coincide. In the elastic stage, the load–area relation is $F \propto a^{1.5}$. When $\omega_{\max}$/h is over 0.367, the elastoplastic deformation occurs. For $\omega_{\max}/h = 0.6$, the first elastoplastic deformation happens in the asperity and the contact area under unloading is larger than the area under loading due to the fact that the deformation cannot be recovered fully which leads to the increase in curvature radius, and hence resulting in the larger contact area. For $\omega_{\max}/h = 0.9$, the second elastoplastic deformation takes place. In the first elastoplastic deformation regime, the load–area relation is $F \propto a^{1.2544}$, and in the second elastoplastic deformation regime, the load–area relation is $F \propto a^{1.1021}$.

The total real contact area and total contact load of the rock joint during unloading can be evaluated as follows:

$$A_r = \int_0^{a_l} n(a)ada \tag{15}$$

where $n(a)$ is the size distribution function of contact asperities in the rough surface and a_l represents the largest contact area of asperity. The total contact load on rough surface is given by

$$F = F_e + F_{ep}^{1} + F_{ep}^{2} = \int_0^{a_{ec}} F_{ne}n(a)da + \int_{a_{ec}}^{a_{epc}} F_{nep}^{1}n(a)da + \int_{a_{epc}}^{a_l} F_{nep}^{2}n(a)da \tag{16}$$

where a_{epc} is the critical elastoplastic contact area, which marks the transition from the first elastoplastic deformation regime to the second elastoplastic deformation regime. It is given by

$$a_{epc} = 0.93a_{ec}\left(\frac{6\omega_c}{\omega_c}\right)^{1.136} = 7.1197a_{ec} \tag{17}$$

Note that Eq. (16) is the foundation for calculating the total contact load on fracture surface. It applies to the unloading conditions of fractured rock, while for loading conditions, a full plastic deformation regime may occur, which should be considered in calculating the total contact

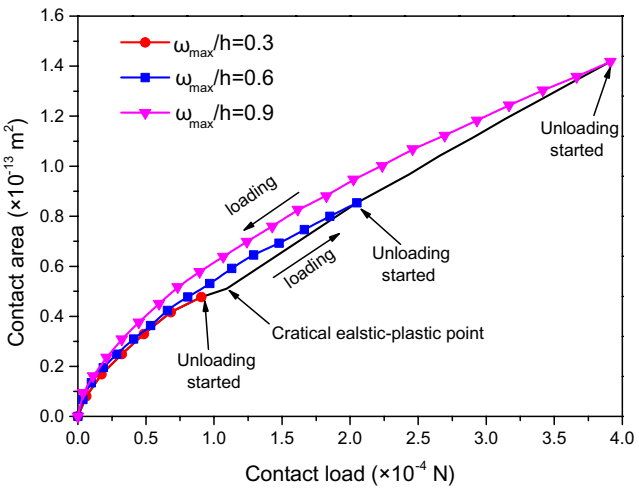

Fig. 10 Relationship between contact area and contact load for a single asperity during loading and unloading

load. Moreover, during the underground excavations, the stress conditions of joint surface in rock masses can be estimated through Eq. (16).

3.2 Correlation Between Permeability and Stress

For porous mediums, it is widely accepted that the permeability evolution is correlated with the effective stress through the exponential function (Shi and Durucan 2004; Liu and Rutqvist 2010; Chen et al. 2015). Therefore, the permeability evolution can be expressed as follows:

$$\frac{k}{k_0} = \exp\left[-3C_f(\sigma - \sigma_0)\right] \tag{18}$$

where k_0 is the initial permeability, C_f is the rock fracture compressibility, σ_0 is the initial effective stress, and σ is the effective stress, which can be obtained by dividing the contact load F by contact area A_r. Combining with Eqs. (16) and (18), we obtain the permeability of rock joint during the unloading process. Since the nature of the preceding loading has a significant influence on the unloading part of the fracture surface contact (Zait et al. 2010), the flow behavior through fractured rock mass varies with the maximum loading stress. For the maximum deformation at the end of the loading phase less than the critical deformation ω_c, only the first item in the right of Eq. (16) should be used. At this stage, the deformation of fracture is elastic and no permeability loss occurs. When the maximum deformation overs ω_c, the elastoplastic contact problem comes into play. This leads to permeability loss during the unloading process, and the second item and even the third item (depending on the regime of elastoplastic deformation) in the right of Eq. (16) should be used to calculate the contact load and then permeability.

3.3 Model Validation

Experimental results and theoretical results are compared to evaluate the usefulness of the proposed model. The morphology parameters of the tested samples are obtained from the 3D morphology scanner system in Sect. 2. The computed processes are as follows:

1. Determine the composite topography and the associated contact case using the morphology data of fracture surface (i.e., the coordinate of surface points obtained from the 3D scanner system).
2. Estimate the size distribution function of contact asperities $n(a)$ and the largest contact asperity area a_l, and calculate the radius of asperity R. In this paper, Gaussian statistical distribution is adopted to describe the asperity height, as shown in Fig. 11.

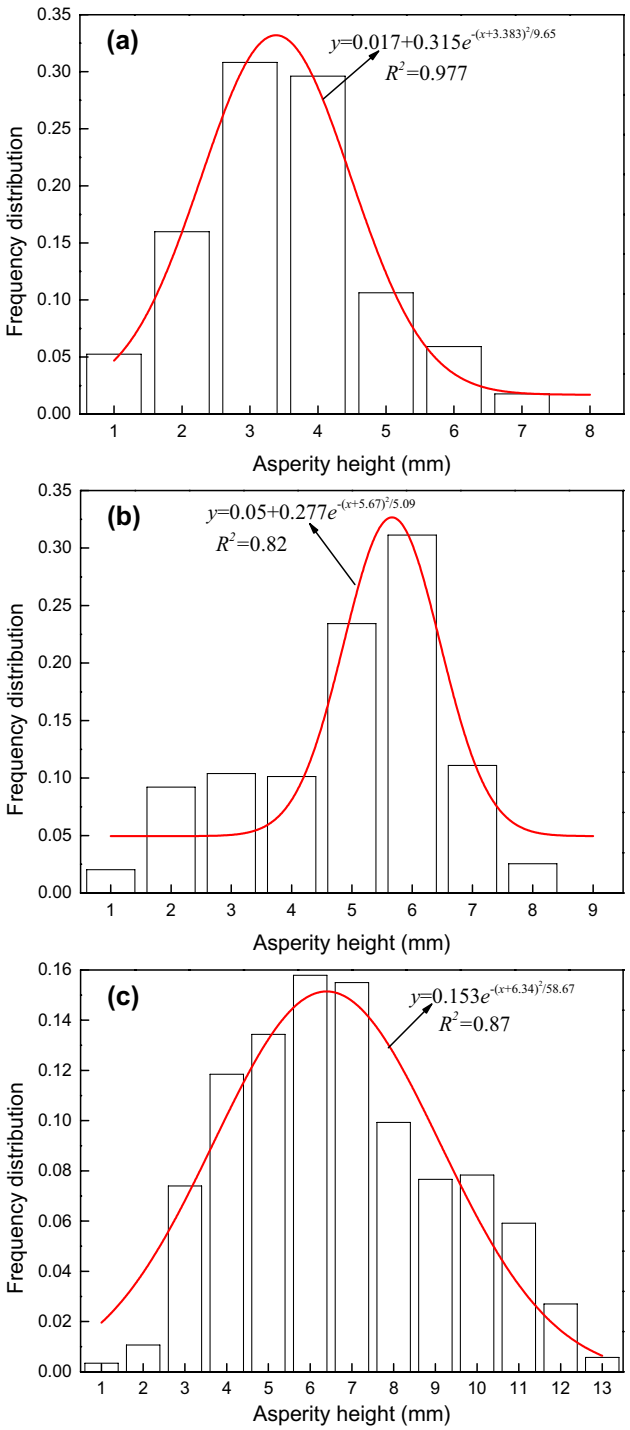

Fig. 11 Size distribution function of asperity height, **a**–**c** corresponding to samples L01, L02, and L03, respectively

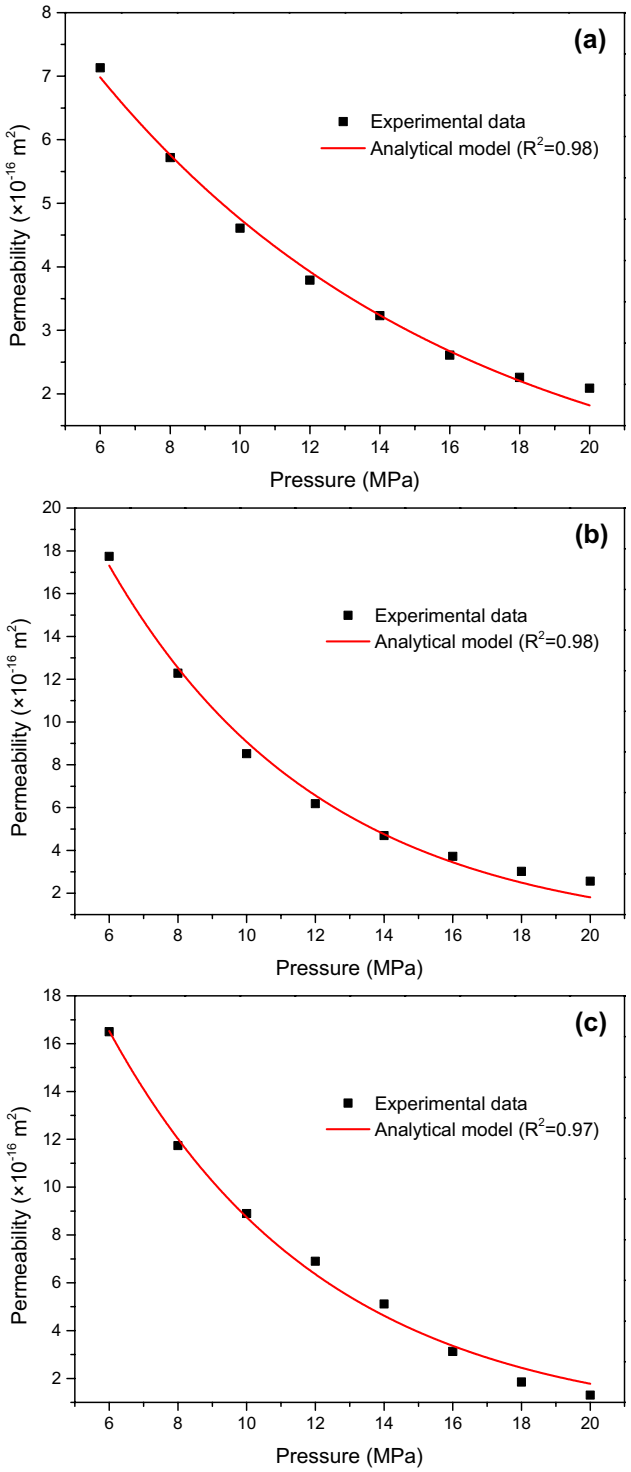

Fig. 12 Comparisons of the predicted curves and the experimental results: **a** sample L01; **b** sample L02; and **c** sample L03

3. Calculate the critical deformation ω_c through Eq. (7), elastic critical contact area a_{ec} through Eq. (8) with $\omega = \omega_c$, and elastoplastic critical contact area a_{epc} through Eq. (17). Then, estimate the deformation regime.
4. Calculate the total contact load and contact area, and estimate the effective stress.
5. Fit the permeability data. Elastic modulus and Poisson's ratio can be determined from the stress–strain curve in uniaxial compression test, in this paper, E is set to 18.7 GPa, and ν is set to 0.33. The values of ω_{max} and C_f are identified by fitting the measured data in Fig. 12. Note that C_f is regarded as constant in the model validation for simplicity.

Both the predicted curves and the experimental results are shown in Fig. 12. Note that the sorption effects are not included in this paper. It can be drawn from Fig. 12 that the evolution of permeability is fairly well captured by our model for the whole unloading process, supporting the usefulness of our model.

4 Conclusions

Underground excavations usually cause stress unloading of the surrounding rock masses, which changes the rock mass permeability significantly. This paper investigates the fluid flow behavior through fractured rock mass under unloading conditions by performing a series of permeability tests on three fractured limestones. Based on the study, several conclusions can be drawn.

1. Permeability and deformation of fractured samples measured under unloading conditions are found to be smaller than those obtained under loading conditions under the same effective stress. The permeability reduction can be attributed to the fracture surfaces deformation and pore space squeeze due to fracture surfaces contact crush and friction slipping. Mutual embedding of fracture surfaces and pulverized particles filling are very difficult to compensate for in the process of unloading, resulting in a significant reduction in permeability.
2. The height statistic parameters were measured to quantify the morphological change of fracture surfaces before and after testing. It is found that the maximum peak height S_p, maximum depth of valleys S_d, maximum height S_h, and arithmetical mean height S_m were all decreased after testing, indicating that the surface roughness decreases as a result of compression due to the confining pressure and scouring due to the flowing water.
3. To describe the flow behavior under the unloading condition, a fractured rock permeability model is developed

by the model of elastoplastic contact between rough surfaces. In the present model, both the effects of the topography of fracture surfaces and the elastoplastic deformations are considered. The proposed approaches are demonstrated by favorable comparisons between measured and analytical results.

Acknowledgements This research was supported by the National Natural Science Foundation of China (No.51374257 and No. 50804060), the Science and Technology Support Project of Guizhou (No. [2020]4Y044) and No. [2018]2787), the Research Fund for Talents of Guizhou University (Grant No. 201901), and the Special Research Funds of Guizhou University (Grant No. 201903). The authors declare that they have no conflict of interest.

References

Brace WF, Walsh JB, Frangos WT (1968) Permeability of granite under high pressure. J Geophys Res 73:2225–2236. https://doi.org/10.1029/JB073i006p02225

Brown SR, Scholz CH (1985) Closure of random elastic surfaces in contact. J Geophys Res: Solid Earth 90(B7):5531–5545

Brown SR, Scholz CH (1986) Closure of rock joints. J Geophys Res: Solid Earth 91(B5):4939–4948

Chang WR, Etsion I, Bogy DB (1987) An Elastic-Plastic Model for the Contact of Rough Surfaces. ASME J Tribol 109:257–263

Chang WR, Etsion I, Bogy DB (1988) Static friction coefficient model for metallic rough surfaces. ASME J Tribol 110:57–63

Chen Y, Cao P, Chen R, Teng Y (2010) Effect of water-rock interaction on the morphology of a rock surface. Int J Rock Mech Min Sci 47(5):816–822

Chen D, Pan ZJ, Ye ZH (2015) Dependence of gas shale fracture permeability on effective stress and reservoir pressure: model match and insights. Fuel 139:383–392

Connell LD (2016) A new interpretation of the response of coal permeability to changes in pore pressure, stress and matrix shrinkage. Int J Coal Geol 162:169–182

Cook NGW (1992) Natural joints in rock: mechanical, hydraulic and seismic behaviour and properties under normal stress. Int J Rock Mech Min SciGeomechAbstr 29(3):198–223

Davy CA, Skoczylas F, Barnichon JD, Lebon P (2007) Permeability of macro-cracked argillite under confinement: gas and water testing. PhysChem Earth Parts A/B/C 32:667–680

Dong JJ, Hsu JY, Wu WJ, Shimamoto T, Hung JH, Yeh EC, Wu YH, Sone H (2010) Stress-dependence of the permeability and porosity of sandstone and shale from TCDP Hole-A. Int J Rock Mech Min Sci 47:1141–1157

Etsion I, Kligerman Y, Kadin Y (2005) Unloading of an elastic–plastic loaded spherical contact. Int J Solids Struct 42(13):3716–3729

Greenwood JA, Williamson JBP (1966) Contact of nominally flat surfaces. Proc R SocLondA 295:300–319

Jiang C, Duan M, Yin G, Wang J, Lu T, Xu J, Zhang D, Huang G (2017) Experimental study on seepage properties, AE characteristics and energy dissipation of coal under tiered cyclic loading. EngGeol 221:114–123

Johnson KL (1985) Contact mechanics. Cambridge University Press, Cambridge

Kogut L, Etsion I (2002) Elastic–plastic contact analysis of a sphere and a rigid flat. ASME J ApplMech 69:657–662

Li B, Jiang YJ, Koyama T, Jing L, Tanabashi Y (2008) Experimental study of the hydro-mechanical behavior of rock joints using a parallel-plate model containing contact areas and artificial fractures. Rock Mech Rock Eng 45:362–375

Li B, Liu RC, Jiang YJ (2019a) An experimental method to visualize shear-induced channelization of fluid flow in a rough-walled fracture. Hydrogeol J 27:3097–3106

Li SC, Gao CL, Zhou ZQ, Li LP, Wang MX, Yuan YC, Wang J (2019b) Analysis on the precursor information of water inrush in karst tunnels: a true triaxial model test study. Rock Mech Rock Eng 52:373–384

Liu HH, Rutqvist J (2010) A new coal-permeability model: internal swelling stress and fracture- matrix interaction. Transp Porous Media 82:157–171

Qiu SL, Feng XT, Xiao JQ, Zhang CQ (2014) An experimental study on the pre-peak unloading damage evolution of marble. Rock Mech Rock Eng 47(2):401–419

Sharifzadeh M, Mitani Y, Esaki T (2008) Rock joint surfaces measurement and analysis of aperture distribution under different normal and shear loading using GIS. Rock Mech Rock Eng 41(2):299–323

Shi J, Durucan S (2004) Drawdown induced changes in permeability of coalbeds: a new interpretation of the reservoir response to primary recovery. Transp Porous Media 56:1–16

Singh KK, Singh DN, Ranjith PG (2015) Laboratory simulation of flow through single fractured granite. Rock Mech Rock Eng 48(3):987–1000

Tang ZC, Jiao YY, Wong LNY (2017) Theoretical model with multi-asperity interaction for the closure behavior of rock joint. Int J Rock Mech Min Sci 97:15–23

Vogler D, Amann F, Bayer P, Elsworth D (2016) Permeability evolution in natural fractures subject to cyclic loading and gouge formation. Rock Mech Rock Eng 49:3463–3479

Wang K, Zang J, Wang G, Zhou A (2014) Anisotropic permeability evolution of coal with effective stress variation and gas sorption: model development and analysis. Int J Coal Geol 130:53–65

Wang CL, Pan L, Zhao Y, Zhang Y, Shen W (2019) Analysis of the pressure-pulse propagation in rock: a new approach to simultaneously determine permeability, porosity, and adsorption capacity. Rock Mech Rock Eng 52:4301–4317

Yang DS, Qi XY, Chen WZ, Wang SG, Yang JP (2018) Anisotropic permeability of coal subjected to cyclic loading and unloading. Int J Geomech 18(8):04018093

Yuan Y, Cheng Y, Liu K, Gan L (2017) A revised Majumdar and Bushan model of elastoplastic contact between rough surfaces. Appl SurfSci 425:1138–1157

Yuan Y, Cheng J, Zhang L (2018) Loading-unloading contact model between three-dimensional fractal rough surfaces. AIP Adv 8:075017. https://doi.org/10.1063/1.5027437

Zait Y, Kligerman Y, Etsion I (2010) Unloading of an elastic–plastic spherical contact under stick contact condition. Int J Solids Struct 47:990–997

Zhang Y, Chai JR (2020) Effect of surface morphology on fluid flow in rough fractures: a review. J Nat Gas SciEng 79:103343

Zhang Z, Zhang R, Xie H, Gao M, Xie J (2016) Mining-induced coal permeability change under different mining layouts. Rock Mech Rock Eng 49(9):3753–3768

Zhang C, Tu S, Zhang L (2017) Analysis of broken coal permeability evolution under cyclic loading and unloading conditions by the model based on the Hertz contact deformation principle. Transp Porous Med 119:739–754

Zhang C, Zhang L, Zhao Y, Wang W (2018) Experimental study of stress–permeability behavior of single persistent fractured coal samples in the fractured zone. J GeophysEng 15:2159–2170

Zhang ZZ, Deng M, Bai JB, Yu XY, Wu QH, Jiang LS (2020) Strain energy evolution and conversion under triaxial unloading

confining pressure tests due to gob-side entry retained. Int J Rock Mech Min Sci 126:104184. https://doi.org/10.1016/j.ijrmms.2019.104184

Zhao YS, Hu YQ, Wei JP, Yang D (2003) The experimental approach to effective stress law of coal mass by effect of methane. Transp Porous Med 53(3):235–244

Zhao YL, Zhang LY, Wang WJ, Tang JZ, Lin H, Wan W (2017) Transient pulse test and morphological analysis of single rock fractures. Int J Rock Mech Min Sci 91:139–154

Zhao Y, He PF, Zhang YF, Wang CL (2019a) A new criterion for a toughness-dominated hydraulic fracture crossing a natural frictional interface. Rock Mech Rock Eng 52:2617–2629

Zhao Y, Wang CL, Zhang YF, Liu Q (2019b) Experimental study of adsorption effects on shale permeability. Nat Resour Res 28(4):1575–1586